Nano Research

Open Access

Research Article

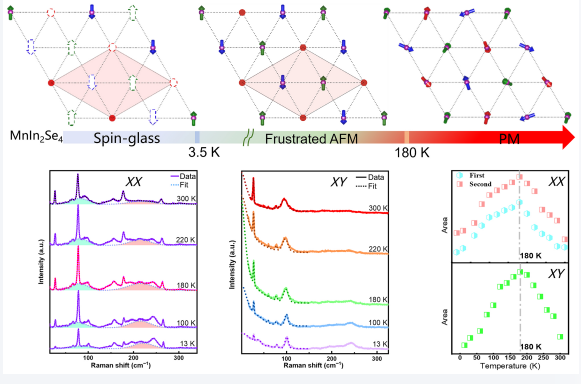
Geometrically frustrated antiferromagnetic order transition in two-dimensional van der Waals semiconductor $MnIn_2Se_4$

Bingbing Lyu[1,2,3,4], Shuo Wang[1], Haiyan Zhu[2], Yupeng Zhu[2], Haimeng Wang[1], Chengzhe Chen[1], Cuiying Hu[1], Yeyang Guo[1], Jihui Fan[1], Xiji Shao[5] ✉, Yuantao Chen[2] ✉, Jifeng Shao[6] ✉, Mingyuan Huang[2] ✉, and Yilin Wang[1,4] ✉

[1] *School of Integrated Circuits, Shandong Key Laboratory of Next-Generation Semiconductor Technology and Systems, Shandong University, Jinan 250100, China*
[2] *Department of Physics, Southern University of Science and Technology, Shenzhen 518055, China*
[3] *School of Physics, Harbin Institute of Technology, Harbin 150001, China*
[4] *Shenzhen Research Institute of Shandong University, Shenzhen 518057, China*
[5] *Department of Physics, School of Intelligent Engineering, Shaoguan University, Shaoguan 512005, China*
[6] *Marine Science and Technology Domain, Beijing Institute of Technology, Zhuhai 519088, China*

Cite this article: *Nano Research*, **2026**, *19*, 94908938. https://doi.org/10.26599/NR.2026.94908938

ABSTRACT: The geometrically frustrated antiferromagnetism, revealing non-mean-field ordering mechanisms through partial order, quantum fluctuations, and criticality, has long been a central focus in condensed matter physics for probing and manipulating novel phases of matter. However, the direct experimental observation of the phase transition associated with this frustrated antiferromagnetic order, termed "hidden order", in two-dimensional systems remains a significant challenge. This is primarily due to the scarcity of suitable candidate materials and the limitations of conventional measurement techniques. Here, we investigate the magnetic properties of $MnIn_2Se_4$, a promising candidate for studying such transitions. Using a combination of polarized Raman spectroscopy, density functional theory (DFT), and Monte Carlo simulations calculations, we observe this geometrically frustrated antiferromagnetism order that persists from the spin-freezing temperature of 3.5 K up to 180 K. This transition is characterized by pronounced magneto-optical scattering phenomena, manifested by two distinct broad spectral regions of continuous magnetic states, with inflection points emerging at 180 K. Additionally, we detect temperature-dependent quasi-elastic scattering (QES) and Fano resonance, further confirming the magnetic order change. The presence of geometrically frustrated interactions in this material provides a natural explanation for the observed extended temperature range of the partial order phase. These findings establish $MnIn_2Se_4$ as a promising material platform for investigating frustration-driven phase transitions and the underlying mechanisms of high-temperature superconductivity and quantum bits. The insights gained into the interplay between thermal fluctuation effects on magnetic interactions may open new avenues for designing functional semiconductor devices with tunable magnetic and topological characteristics.



KEYWORDS: geometrically frustrated antiferromagnetism, two-dimensional van der Waals magnetic materials, polarized Raman spectroscopy, phase transition

1 Introduction

Two-dimensional magnetic materials provide an ideal platform for exploring novel quantum phases arising from enhanced quantum fluctuations and spin frustration, positioning them at the forefront of condensed matter physics [1–5]. In recent years, research in this field has increasingly focused on manganese-containing III/V–VI systems [6–9], such as $MnBi_2Te_4$ [10–12], due to their unique

Received: April 24, 2026; **Revised:** June 10, 2026
Accepted: June 15, 2026

✉Address correspondence to Xiji Shao, shaoxj@mail.sustech.edu.cn; Yuantao Chen, 12231305@mail.sustech.edu.cn; Jifeng Shao, jfshao@bit.edu.cn; Mingyuan Huang, huangmy@sustech.edu.cn; Yilin Wang, yilinwang@email.sdu.edu.cn

combination of topological insulator properties and magnetic order. Among these materials, $MnIn_2Se_4$ stands out as one of the few two-dimensional magnetic semiconductors with a direct bandgap—a property that is relatively rare in the realm of two-dimensional magnetic materials [13–18]. Unlike Kitaev magnets such as α-$RuCl_3$ [19, 20], which are often plagued by pervasive stacking defects, or triangular lattice systems like $NaCrO_2$ that lack clean cleavage planes [21, 22], $MnIn_2Se_4$ uniquely offers a pristine, exfoliable van der Waals layered structure and a favorable optical bandgap of ~ 1.38 eV [16–18]. This combination ensures both clean exfoliation and optical accessibility while preserving a high geometric frustration index (f > 10) [15–18], establishing it as an ideal system to investigate hidden orders without the interference of stacking disorder or substrate effects. This unique characteristic endows $MnIn_2Se_4$ with significant potential for applications in optoelectronic heterojunctions, magneto-optical devices, and photocatalysis [13, 14, 23–25]. Prior studies have reported that $MnIn_2Se_4$ exhibits spin freezing phenomena below 3.5 K, while antiferromagnetic (AFM) ordering has been speculated to emerge above this temperature [24, 26–28]. However, there remains a critical lack of experimental data investigating the magnetic orders above 3.5 K, as well as the magnetic order transition of $MnIn_2Se_4$ with temperature. A major obstacle is the inability of conventional probing techniques to resolve hidden magnetic order transitions and their intrinsic magnetic excitations. Raman spectroscopy whose spectral response is highly sensitive to spin–phonon coupling and magnetic orders can effectively detect hidden magnetic orders even with zero net magnetization [25, 29–32], thus offering a unique perspective for elucidating the microscopic magnetism of $MnIn_2Se_4$.

In this study, we employ polarized Raman spectroscopy to characterize the magneto-optical scattering signatures of $MnIn_2Se_4$ across a broad temperature range. We observe that two broad spectral regions exhibit a marked inflection point in their temperature-dependent evolution at approximately 180 K. We attribute the observed spectral evolution to the interplay between thermal energy and magnetic exchange interactions. At temperatures below 3.5 K, the random occupation of metal sites by Mn^{2+} ions reinforce magnetic frustration, leading to spin freezing into a glassy state where thermal fluctuations are largely suppressed. Within the temperature range from 3.5 to 180 K, thermal fluctuations remain weaker than the intralayer exchange interactions, thereby stabilizing a partial long-range magnetically ordered state in the system. The evolution of spin configurations with increasing temperature across this interval was systematically investigated using density functional theory (DFT) and Monte Carlo simulations. Our calculation results demonstrate the formation of a fully compensated frustrated antiferromagnetic order on a triangular lattice within this temperature regime. Furthermore, we observed quasi-elastic scattering (QES) centered at 0 cm^{-1}, whose intensity varies with temperature, further confirming the magnetic order change at 180 K. The QES is strongly coupled with phonons, forming Fano resonance. With increasing temperature, the Fano peak exhibits a significant blue shift and an increase in its full-width at half-maximum (FWHM). This behavior is related to the in-plane relative motion between Mn-connected Se atoms. Our results highlight the complex interplay between thermal fluctuations and interlayer/intralayer magnetic interactions in $MnIn_2Se_4$, offering new insights for the design of functional magnetic devices.

2 Experimental section

All the samples of the Raman spectroscopy were arranged by mechanical exfoliation on Si substrates with a layer of 90 nm SiO_2. The thickness of the samples was measured by atomic force microscopy. In a home-built micro-Raman system, the temperature dependent Raman spectra of $MnIn_2Se_4$ samples were measured at 13 and 300 K using a Janis cryostat. The excitation light was 632.8 nm line of He Ne laser in the whole measurements. In order to avoid sample heating or damage, the laser power was kept at below 100 μW. Laser beam passing 20× microscope objective lens focused the $MnIn_2Se_4$ film sample. The scattered light was collected by the same objective lens, ensuring high accuracy. The Rayleigh scattering was suppressed by two ultra-narrow notch filters, and then dispersed by the Horiba ihr 550 spectrometer, with a grating of 1200 and 1800 grooves/mm, detected by the liquid nitrogen cooled charge-coupled device (CCD) detector. For the measurement of polarized Raman, the polarization analyzer was used to convert the scattered light from parallel (XX) to vertical (XY). The optical path primarily utilized Bragg bandpass filters (BPFs) and Bragg notch filters (BNFs) for filtering. The low-temperature (from 1.7 to 130 K) Raman measurements were provided by an Attocube autoDRY 2100 closed-cycle cryostat. The magnetization data of $MnIn_2Se_4$ samples was mainly measured using a Quantum Design magnetic property measurement system (MPMS-3) with the maximum field of 7 T.

Single crystals of $MnIn_2Se_4$ were grown by the chemical vapor transport method [14, 17]. We used I_2 as the transport agent and Mn (purity 99.9%), In (purity 99.9%), and Se (purity 99.9%) powder as the precursors. Transport agent and precursors were mixed and sealed into a silica tube under vacuum. After heating with a source temperature of 860 °C and temperature gradient of 60 °C for one week, millimeter sized single crystals were obtained.

3 Results and discussion

The $MnIn_2Se_4$ single crystal features a van der Waals-type layered structure with the rhombohedral space group $R\bar{3}m$. As shown in Fig. 1(a), the centrosymmetric unit is composed of 12 almost closed selenium layers, and the hexagonal lattice parameters $a = b =$ 0.4051 nm, c = 3.946 nm. The Mn^{2+} and In^{3+} sites are located in the tetrahedral and octahedral gaps between these layers [18, 29, 33]. Viewed along the c-axis, as shown in Fig. 1(b), the Mn atoms form a geometrically frustrated triangular lattice with competing exchange interaction paths. To confirm the crystal structure of $MnIn_2Se_4$, we performed X-ray diffraction (XRD) on a flat single-crystal sample and only see (00l) diffraction peaks without any impurity signals, as shown in Fig. 1(c). Additionally, energy-dispersive X-ray spectroscopy (EDS) analysis (Fig. S1 in the Electronic Supplementary Material (ESM)) quantifies the elemental composition and verifies the high crystallinity of the sample. Furthermore, this material can be easily fabricated into few-layer structures and exhibits remarkable stability under ambient conditions (as shown in Figs. S2(a) and S2(b) in the ESM), which is highly advantageous for subsequent spectroscopic characterization. Due to the triangular lattice structure of $MnIn_2Se_4$ and the competing exchange interactions between Mn–Mn atoms, this material exhibits different magnetic states as temperature changes. For example, at temperatures below 3.5 K, where thermal fluctuations are significantly suppressed, the random occupation of metal sites by Mn^{2+} ions enhances magnetic frustration. This, in

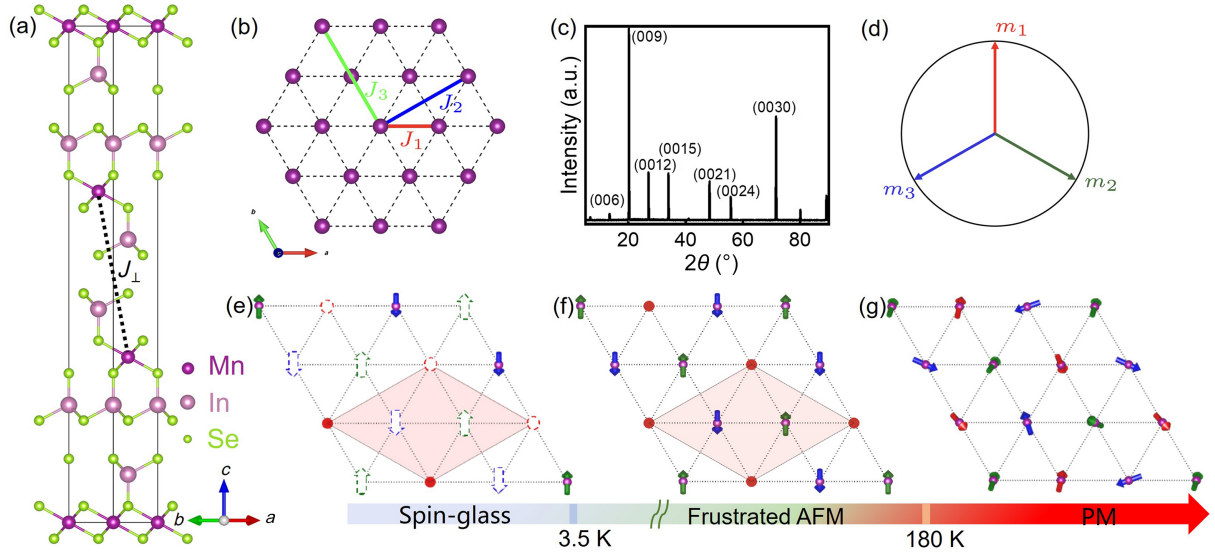


Figure 1 Crystal structure of $MnIn_2Se_4$ crystal and evolution of magnetic configurations with temperature. (a) Crystal structure of the $MnIn_2Se_4$ material and schematic diagram of $J_\perp$. (b) Schematic illustration of the exchange interaction paths, including the first-nearest-neighbor exchange interaction (J_1), J_2, and J_3. (c) XRD patterns of the $MnIn_2Se_4$ bulk crystal. (d) Spin-frame vectors for the magnetic configurations corresponding to (e)–(g) below. (e) Below 3.5 K, the system enters a spin-glass state. The position of the dashed arrow indicates the randomness of the spin orientation. The shaded area indicates a magnetic unit cell, inside which the magnetic order parameter is displayed. (f) In the temperature range from 3.5 to 180 K, the magnetic configuration is a frustrated AFM order. (g) Above 180 K, the system transitions to a PM state.

conjunction with antiferromagnetic interactions, promotes the formation of a spin-glass state, as illustrated in Fig. 1(e), a phenomenon that has been corroborated by previous studies [15, 24, 26–28, 34]. As the temperature increases above 3.5 K, the enhanced thermal energy destabilizes the spin-glass state. The specific exchange interactions combined with the geometrically frustrated crystal structure may lead to the emergence of an AFM order, depicted in Fig. 1(f). With a further rise in temperature, the increasingly dominant thermal agitation ultimately disrupts the antiferromagnetic order, driving the material into a paramagnetic (PM) state, as shown in Fig. 1(g). Figure 1(d) shows the spin-frame vectors corresponding to the magnetic configurations presented in Figs. 1(e)–1(g). To elucidate this temperature-dependent magnetic evolution, the following experiments were performed.

Prior to conducting Raman spectroscopy measurements, the magnetic properties of the $MnIn_2Se_4$ single crystal were systematically characterized using a Quantum Design magnetic property measurement system to confirm overall magnetic behavior, as shown in Fig. S3 in the ESM. The results indicate that below 3.5 K, $MnIn_2Se_4$ exhibits canonical spin glass behavior consistent with previous findings [35–37], accompanied by pronounced out-of-plane magnetic anisotropy. However, no additional magnetic transitions were observed between 3.5 and 300 K. This absence of a clear signature in magnetic susceptibility $\chi(T)$ aligns with hidden-order transitions in frustrated systems [38, 39], where DC magnetization, which probes only the uniform spin susceptibility, typically misses short-range correlated states, while Raman scattering remains sensitive to the associated lattice and spin correlations. To further investigate the structure and magnetic properties of the thin layer (~ 10 nm) $MnIn_2Se_4$, we conducted a meticulous analysis using Raman spectroscopy over an extensive temperature range from 1.7 to 300 K. The temperature-dependent Raman spectra measured from 13 to 300 K are presented in Fig. S4 in the ESM. This investigation employed both *XX* and cross (*XY*) polarization configurations to obtain the vibrational characteristics, and the corresponding schematic diagram of setup is shown in Fig. 2(a). Figure 2(b) shows the temperature-dependent polarized Raman spectra acquired at 13 and 300 K. These spectra reveal nine well-resolved and prominent phonon modes within the 5–300 cm^{-1} range. The symmetry attributes of these Raman modes are clearly discernible from the spectra. Specifically, the phonon modes situated at 27 and 244 cm^{-1} are designated as E_g modes, whereas the remaining modes are attributed to A_g Raman vibrational modes. It is worth noting that the apparent polarization dependence of the E_g intensities in Fig. 2(b) primarily arises from the overlap with underlying, strongly polarization-sensitive scattering backgrounds, namely, quasi-elastic scattering and a magnetic continuum, rather than from intrinsic anisotropy of the E_g phonons themselves. To further elucidate the polarization-dependent behavior of specific modes, the intensities of the A_g vibrational mode at 79 cm^{-1} and the E_g vibrational mode at 244 cm^{-1} as functions of the polarization angle are plotted in Figs. 2(c) and 2(d), respectively. To delve into the origins of these observed Raman modes, we employed first-principles computational simulations using a rigorous and established method [40–42]. A comprehensive summary of the symmetry characteristics and corresponding calculated frequencies for all Raman vibrational modes is provided in Table S1 in the ESM. The E_g mode at 27 cm^{-1} is associated with the in-plane relative motion between the upper and lower layers of the outermost Se–In atoms. In contrast, the dominant A_g mode at 79 cm^{-1} corresponds to the breathing mode of the Se–In–Se layers. In addition to the sharp phonon modes, two broad spectral features are observed in the 50–125 and 125–275 cm^{-1} ranges within the *XX* polarization channel. This observed broad, diffuse line-shape—a fingerprint of a magnetic continuum spectrum characteristic of low-dimensional or frustrated systems with fractionalized spin excitations (e.g., $NiPS_3$, VI_3, and α-$RuCl_3$)—suggests a potential origin in magnetic continua. Such a magnetic continuum can, via magnetoelastic coupling, exert a continuous perturbation on the lattice. The resulting deformation modulates the magnetic exchange interaction, thereby inducing the observed broadband phonon response [43–46].

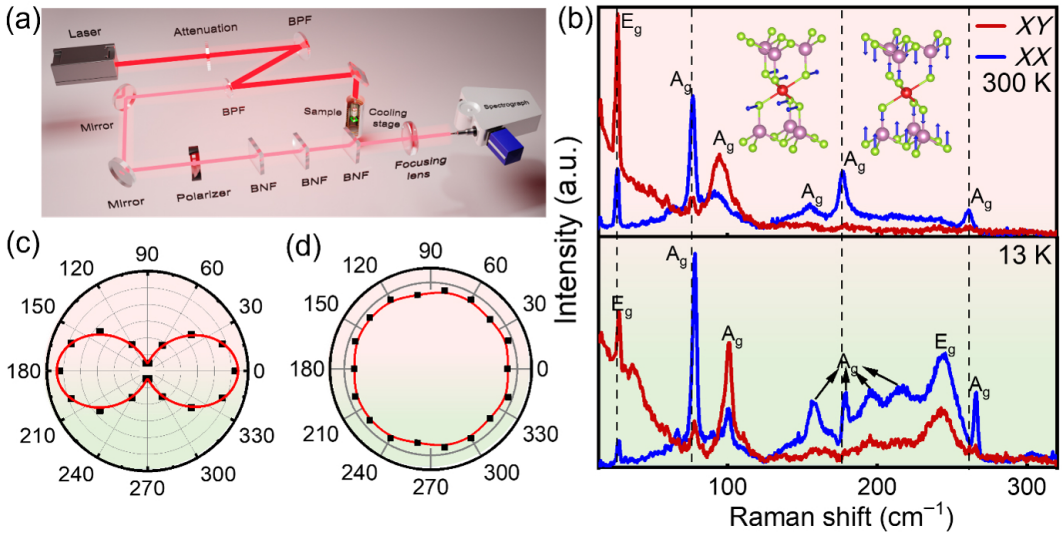


Figure 2 (a) Schematic diagram of the polarized Raman spectroscopy setup. (b) Raman spectra in the parallel-polarization channel (*XX*, blue) and cross-polarization channel (*XY*, red) at 300 and 13 K. The polar intensity plot as a function of polarization angle, which represents the angle between the polarization analyzer and the polarization of the incident light, for (c) the dominant A_g mode at 79 cm^{-1} and (d) E_g mode at 244 cm^{-1} at 13 K.

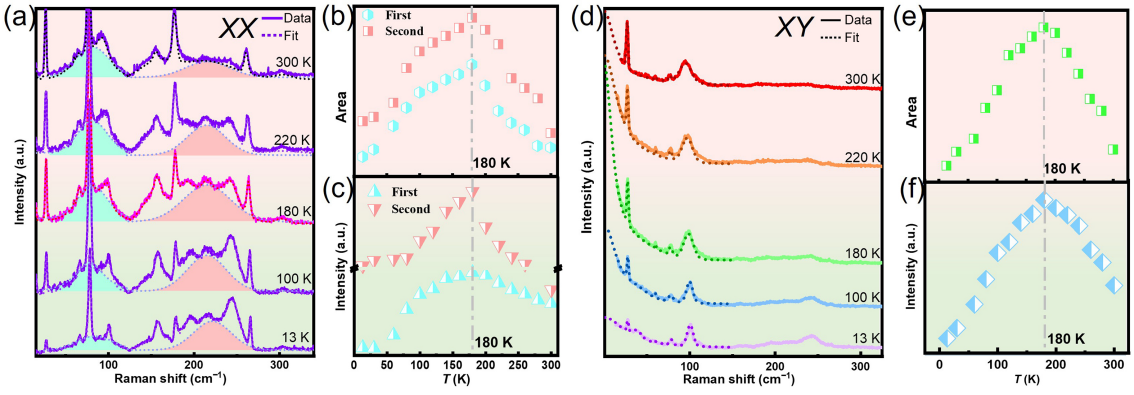


Figure 3 (a) The selected temperature-dependent polarization Raman spectra from the *XX* channel of $MnIn_2Se_4$ material, along with their corresponding fitted data lines. The solid lines denote the raw experimental data, whereas the dashed lines depict the data following fitting procedures. The region delineated in cerulean blue corresponds to the integral area encompassing the first magnetic continuum state, and the region delineated in tangerine orange corresponds to the integral area encompassing the second magnetic continuum state. (b) Statistical data illustrating the temperature dependence of the integral areas of the first and second magnetic continuum states. (c) Statistical data depicting the temperature-dependent peak intensities of the first and second magnetic continuum states. (d) Selected temperature-dependent polarization Raman spectra obtained from the *XY* channel of the $MnIn_2Se_4$ material and their corresponding fitted data lines. Solid lines indicate the raw experimental data, while dashed lines represent the data after fitting procedures. (e) Statistical plot depicting the temperature dependence of the integrated area subsequent to the fitting of QES spectra. (f) Statistical plot illustrating the temperature dependence of the intensity of QES spectra.

To delve into the magnetic behavior of $MnIn_2Se_4$ in detail, Fig. 3(a) presents the temperature-dependent Raman spectra of the $MnIn_2Se_4$ material in the *XX* polarization channel. The solid lines correspond to the raw data, while the dashed lines represent the fitted data. The cyan and orange-red sections depict the integrated areas of the first and second magnetic continuum states, respectively. As observed in Fig. 3(a), it can be clearly seen that the strength of the magnetic continuity increases with the increase of temperature, and then decreases continuously after 180 K, and it still exists at room temperature. To further elucidate this trend, Figs. 3(b) and 3(c) present the processed statistical graphs of the integrated areas and intensities of the two magnetic continuum states following the fitting of the corresponding data. These graphical representations offer a clearer visualization of the transition point at 180 K. The observed phenomenon indicates that a magnetic order transition occurs in the $MnIn_2Se_4$ at this temperature.

Concurrently, a peak centered with 0 cm^{-1} can be observed from the *XY* channel polarization spectra in Fig. 2(b), which is named QES. This peak is characteristic of low-temperature magnetic systems and is instrumental in characterizing the magnetic fluctuations within the material, as well as signaling the onset of magnetic or structural phase transitions [44, 47, 48]. The single-crystal XRD pattern (Fig. 1(c)), exhibiting only (00*l*) diffraction peaks with no impurity signals, and the precise 1:2:4 stoichiometry confirmed by EDS (Fig. S1 in the ESM) effectively rule out defect-related relaxational modes. Furthermore, the strong correlation between the QES intensity and the onset of magnetic order suggests an intrinsic magnetic origin, rather than charge density fluctuations, which are negligible in this system. To elucidate the interplay between QES and magnetic transitions, we conducted temperature-dependent polarized Raman measurements in the *XY* channel, as depicted in Fig. 3(d). Figures 3(e) and 3(f) present the statistical analyses of the integrated areas and intensities of the QES at

different temperatures, respectively. Detailed procedures for QES peak fitting are provided in Fig. S6 in the ESM. These analyses unequivocally show that the QES intensity increases with rising temperature, reaches a maximum at 180 K, and then declines. Notably, Fig. 3(d) reveals that the QES intensity is relatively subdued at lower temperatures, which can be ascribed to the dampening of spin fluctuations due to the robust super-exchange interactions inherent in the disordered state. Upon elevation of temperature, there is a concomitant increase in thermal fluctuations and a concomitant reduction in the efficacy of exchange interactions. At the critical temperature of 180 K, these thermal fluctuations and exchange interactions achieve a state of equilibrium, precipitating the emergence of a novel magnetic ordering. Beyond this threshold, the temperature increment results in the predominance of thermal fluctuations, concurrent with a progressive attenuation of exchange interactions, which can no longer effectively oppose the thermal perturbations, culminating in a transition to a paramagnetic, disordered state. In tandem with this thermal elevation, the Raman spectral shift is observed to migrate towards lower wavenumbers, a phenomenon that is indicative of lattice dilation and a concomitant reduction in the strength of exchange interactions. Supporting evidence for these observations is delineated within Fig. S3 in the ESM. The temperature-dependent trend of QES aligns with that of the magnetic continuum, further substantiating the occurrence of a magnetic order transition at 180 K in $MnIn_2Se_4$.

Another interesting phenomenon which can be seen from the polarization Raman spectrum in Fig. 2(b) is that the shapes of the Raman peaks at 100, 158, 179, 195, 216, 243, and 266 cm^{-1} all show asymmetric linearity and broadening. This is mainly a Fano resonance feature from the coupling between discrete phonon states and continuum states [44, 47–49]. Here, we choose the peak centered at 100 cm^{-1} as an example to study its temperature-dependent evolution. This mode corresponds to the Mn-connected Se breathing mode (see Table S1 in the ESM). As shown in Fig. 4(a), after deducting the continuum, the peaks at different temperatures are extracted in the range of 70–120 cm^{-1}. The black line is the experimental data, and the red line is the fitted data. The results are fitted well with the Fano formula [49]

$$I(\omega) = I_0 \frac{[1+(\omega-\omega_0)/qI]^2}{1+[(\omega-\omega_0)/I]^2} \quad (1)$$

where $I(\omega)$, I_0, ω, ω_0, I, and q are the intensity of the Fano resonance peak, the intensity of the initial phonon peak, the phonon frequency responsible for the Fano resonance, the phonon frequency, FWHM, and asymmetry parameter, respectively. The FWHM and Raman shift extracted from the fitting are plotted as a function of temperature in Figs. 4(b) and 4(c). The FWHM increases continuously with the increase of temperature, and the increase rate of FWHM becomes smaller obviously after reaching 180 K. As can be seen from the evolution of formants, there is a turning point at 180 K. In addition, the Raman center position of 100 cm^{-1} shifts to lower wavenumbers with increasing temperature, which can be seen in Fig. 4(a). Clearly, the FWHM, which represents the strength of the coupling, reaches its highest value at which the QES intensity and the magnetic continuum ranging from 125 to 275 cm^{-1} go to the maximum. Therefore, we can conclude that the Fano resonance is arising from the coupling between the phonon and magnetic continuum states.

The observed spectral evolution, which includes two magnetic

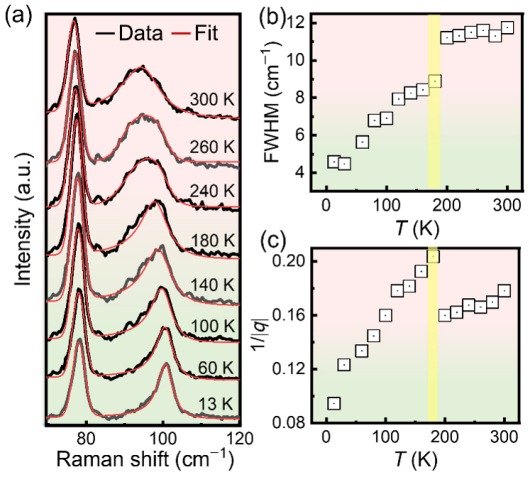


Figure 4 (a) After subtracting the magnetic continuum states, the Raman peaks that exhibit temperature dependence within the wavelength range from 70 to 120 cm^{-1} are presented. The black line represents the raw data, while the red line denotes the fitted data. (b) FWHM and (c) Raman shift extracted from the fitting are plotted as a function of temperature.

continuum states, a QES and Fano resonance peaks, is attributed to the interplay between thermal energy and magnetic exchange interactions. Below the spin glass freezing temperature (~ 3.5 K), the random occupation of metal sites by Mn^{2+} ions introduces disorder in the exchange pathways, leading to a distribution of exchange constants, consistent with prior reports [23–28]. This structural disorder reinforces magnetic frustration and promotes the freezing of spins into a glassy state, with the corresponding magnetic configuration shown in Fig. 1(e), where the dashed lines at Mn sites represent uncertain spin orientations. Under this condition, thermal fluctuations are largely suppressed.

Within the temperature range from 3.5 to 180 K, thermal fluctuations remain weaker than the intralayer exchange interactions, thereby stabilizing a local long-range magnetic ordered state. Combined DFT and Monte Carlo simulations further reveal that the magnetic ground state corresponding to this order is a geometrically frustrated antiferromagnetic configuration on a triangular lattice. Our calculations indicate that the interlayer exchange interaction ($J_\perp$) is two orders of magnitude weaker than the dominant intralayer nearest-neighbor coupling, and is thus negligible. In contrast, the in-plane interactions remain antiferromagnetic up to the third-nearest neighbor, with a specific energy hierarchy of third-nearest-neighbor exchange interaction (J_3) > second-nearest-neighbor exchange interaction (J_2), leading to a geometrically frustrated AFM state, whose corresponding spin configuration is depicted in Fig. 1(f). This frustration, coupled with an out-of-plane magnetic easy axis—as supported by both magnetic anisotropy energy calculations and experimental susceptibility measurements—collectively promotes non-collinear spin arrangements. Detailed computational parameters and procedures are provided in Fig. S7 in the ESM. Notably, this phenomenon manifests as submicroscopic-scale characteristic signatures, whose detection relies on high-sensitivity optical characterization techniques. No distinct magnetic transition was observed in the bulk magnetic susceptibility measurements. This phenomenon may be attributed to the weak magnetic coupling in this material, where the macroscopic magnetic response exhibits insensitivity to external perturbations (such as temperature or magnetic field), whereas Raman spectroscopy provides exceptional sensitivity to subtle shifts

in lattice vibration modes associated with magnetic excitations.

4 Conclusions

In conclusion, we have conducted a comprehensive investigation of the lattice and geometrically frustrated antiferromagnetic phase transitions within $MnIn_2Se_4$ material through a systematic series of Raman spectroscopic measurements. Our study has, for the first time, unequivocally identified the active vibrational modes and magnetic order transition points of $MnIn_2Se_4$. Temperature-dependent polarized Raman spectroscopy has unveiled the presence of a magnetic continuum and QES in $MnIn_2Se_4$, with the peak intensity observed at 180 K. This magnetic transition is attributed to the interplay between thermal energy and magnetic exchange interactions. Within the temperature interval from 3.5 to 180 K, the system sustains a local long-range magnetic ordered state, as the thermal fluctuations remain subordinate to the intralayer exchange interactions. This regime fosters the emergence of a distinctive magnetic phase. Comprehensive analysis combining DFT and Monte Carlo simulations identifies this magnetic order as a geometrically frustrated antiferromagnetic sequence on a triangular lattice. Subsequently, as thermal perturbations become increasingly dominant and exchange interactions continue to decline, they become insufficient to counteract the thermal disruptions, ultimately resulting in a paramagnetic, disordered state. This research not only advances fundamental understanding of this III/V–VI systems material magnetism but also paves the way for engineering high-performance spintronic devices with tailored magnetic and optical properties.

Electronic Supplementary Material: Supplementary material (additional characterization results and Figs. S1–S7) is available in the online version of this article at https://doi.org/10.26599/NR.2026.94908938.

Data availability

All data needed to support the conclusions in the paper are presented in the manuscript and the ESM. Additional data related to this paper may be requested from the corresponding author upon request.

Acknowledgements

We would like to thank Prof. Jinwei Rao from Shandong University for helpful discussions. This research was supported by the National Natural Science Foundation of China (Nos. 12304042 and 12574197), Guangdong Province Basic and Applied Basic Research Foundation (Nos. 2023A1515110508, 2024A1515030118, and 2025A1515012311), Guangdong Provincial Quantum Science Strategic Initiative (No. GDZX2301008), Shenzhen Science and Technology Program (No. JCYJ20250604124231040), the Startup Funding from Shaoguan University (No. 440/9900064706), the Solid State Physics Teaching Steering Committee of the Ministry of Education Teaching Reform Project (No. JZW-24-GT-03), and project (Nos. ZR2023ZD10 and ZR2024QA187) supported by Shandong Provincial Natural Science Foundation.

Declaration of competing interest

The authors declare no competing interests.

Author contribution statement

B. B. L., Y. L. W. and M. Y. H. conceived the project. B. B. L. and J. F. S. designed and performed the experiments. Y. P. Z. and H. M. W. provided and characterized the samples. S. W., C. Z. C., C. Y. H., Y. Y. G., and J. H. F. conducted the Raman measurements and fitting. H. Y. Z., Y. T. C., and X. J. S. provided the theoretical support. All authors discussed the results and co-wrote the paper.

Use of AI statement

None.

References

[1] Burch, K. S.; Mandrus, D.; Park, J. G. Magnetism in two-dimensional van der Waals materials. *Nature* **2018**, *563*, 47–52.

[2] Kang, L. X.; Ye, C.; Zhao, X. X.; Zhou, X. Y.; Hu, J. X.; Li, Q.; Liu, D.; Das, C. M.; Yang, J. F.; Hu, D. Y. et al. Phase-controllable growth of ultrathin 2D magnetic FeTe crystals. *Nat. Commun.* **2020**, *11*, 3729.

[3] Shao, Y. T.; Das, S.; Hong, Z. J.; Xu, R. J.; Chandrika, S.; Gómez-Ortiz, F.; García-Fernández, P.; Chen, L. Q.; Hwang, H. Y.; Junquera, J. et al. Emergent chirality in a polar meron to skyrmion phase transition. *Nat. Commun.* **2023**, *14*, 1355.

[4] Tang, B. J.; Wang, X. W.; Han, M. J.; Xu, X. D.; Zhang, Z. W.; Zhu, C.; Cao, X.; Yang, Y. M.; Fu, Q. D.; Yang, J. Q. et al. Phase engineering of Cr_5Te_8 with colossal anomalous Hall effect. *Nat. Electron.* **2022**, *5*, 224–232.

[5] Dainone, P. A.; Prestes, N. F.; Renucci, P.; Bouché, A.; Morassi, M.; Devaux, X.; Lindemann, M.; George, J. M.; Jaffrès, H.; Lemaitre, A. et al. Controlling the helicity of light by electrical magnetization switching. *Nature* **2024**, *627*, 783–788.

[6] Wang, L.; Shi, Y. P.; Liu, M. F.; Zhang, A.; Hong, Y. L.; Li, R. H.; Gao, Q.; Chen, M. X.; Ren, W. C.; Cheng, H. M. et al. Intercalated architecture of MA_2Z_4 family layered van der Waals materials with emerging topological, magnetic and superconducting properties. *Nat. Commun.* **2021**, *12*, 2361.

[7] Xu, X. L.; Yang, S. Q.; Wang, H.; Guzman, R.; Gao, Y. C.; Zhu, Y. Z.; Peng, Y. X.; Zang, Z. H.; Xi, M.; Tian, S. J. et al. Ferromagnetic–antiferromagnetic coexisting ground state and exchange bias effects in $MnBi_4Te_7$ and $MnBi_6Te_{10}$. *Nat. Commun.* **2022**, *13*, 7646.

[8] Zhan, F. Y.; Qin, Z.; Xu, D. H.; Zhou, X. Y.; Ma, D. S.; Wang, R. Design of antiferromagnetic second-order band topology with rotation topological invariants in two dimensions. *Nano Lett.* **2024**, *24*, 7741–7747.

[9] Guo, H.; Bai, C. Y.; Zhu, K.; Lv, S. H.; Zhai, Z. Y.; Qu, J. Y.; Xian, G. Y.; Han, Y. C.; Hu, G. J.; Qi, Q. et al. Controllable synthesis of high-quality magnetic topological insulator $MnBi_2Te_4$ and $MnBi_4Te_7$ multilayers by chemical vapor deposition. *Nano Lett.* **2024**, *24*, 15788–15795.

[10] Liu, C.; Wang, Y. C.; Li, H.; Wu, Y.; Li, Y. X.; Li, J. H.; He, K.; Xu, Y.; Zhang, J. S.; Wang, Y. Y. Robust axion insulator and Chern insulator phases in a two-dimensional antiferromagnetic topological insulator. *Nat. Mater.* **2020**, *19*, 522–527.

[11] Qiu, J. X.; Tzschaschel, C.; Ahn, J.; Gao, A. Y.; Li, H. C.; Zhang, X. Y.; Ghosh, B.; Hu, C. W.; Wang, Y. X.; Liu, Y. F. et al. Axion optical induction of antiferromagnetic order. *Nat. Mater.* **2023**, *22*, 583–590.

[12] Lin, W. Y.; Feng, Y.; Wang, Y. C.; Zhu, J. J.; Lian, Z. C.; Zhang, H. Y.; Li, H.; Wu, Y.; Liu, C.; Wang, Y. H. et al. Direct visualization of edge state in even-layer $MnBi_2Te_4$ at zero magnetic field. *Nat. Commun.* **2022**, *13*, 7714.

[13] Liang, H.; Feng, T.; Tan, S. D.; Zhao, K. L.; Wang, W.; Dong, B. H.; Cao, L. X. Two-dimensional (2D) $MnIn_2Se_4$ nanosheets with porous structure: A novel photocatalyst for water splitting without sacrificial agents. *Chem. Commun.* **2019**, *55*, 15061–15064.

[14] Yang, J. H.; Zhou, Z. Q.; Fang, J. Z.; Wen, H. Y.; Lou, Z.; Shen, G. Z.; Wei, Z. M. Magnetic and transport properties of a ferromagnetic layered semiconductor $MnIn_2Se_4$. *Appl. Phys. Lett.* **2019**, *115*, 222101.
[15] Choi, J.; Choi, S. L.; Kim, B. S.; Hong, S. C.; Lee, H. W.; Choi, J.; Choi, S.; Hwang, Y.; Um, Y. H. Magnetic and optical properties of $MnIn_2Se_4$ single crystal. *J. Korean Phys. Soc.* **2004**, *45*, 672–674.
[16] Neumann, H.; Bellabarba, C.; Khan, A.; Riede, V. Optical properties of $MnIn_2Se_4$. *Cryst. Res. Technol.* **1986**, *21*, K21–K24.
[17] Döll, G.; Lux-Steiner, M. C.; Kloc, C.; Baumann, J. R.; Bucher, E. Chemical vapour transport and structural characterization of layered $MnIn_2Se_4$ single crystals. *J. Cryst. Growth* **1990**, *104*, 593–600.
[18] Range, K. J.; Klement, U.; Döll, G.; Bucher, E.; Baumann, J. R. Notizen: The crystal structure of $MnIn_2Se_4$, a ternary layered semiconductor. *Z. Naturforsch. B* **1991**, *46*, 1122–1124.
[19] Banerjee, A.; Bridges, C. A.; Yan, J. Q.; Aczel, A. A.; Li, L.; Stone, M. B.; Granroth, G. E.; Lumsden, M. D.; Yiu, Y.; Knolle, J. et al. Proximate Kitaev quantum spin liquid behaviour in a honeycomb magnet. *Nat. Mater.* **2016**, *15*, 733–740.
[20] Zhang, H. D.; McGuire, M. A.; May, A. F.; Chao, H. Y.; Zheng, Q.; Chi, M. F.; Sales, B. C.; Mandrus, D. G.; Nagler, S. E.; Miao, H. et al. Stacking disorder and thermal transport properties of α-$RuCl_3$. *Phys. Rev. Mater.* **2024**, *8*, 014402.
[21] Huang, B. W.; Hao, P. L.; Sheng, Z. G. Short-range spin order and spin–phonon coupling in $NaCrO_2$ revealed by terahertz spectra. *Phys. Rev. B* **2026**, *113*, 094435.
[22] Tomiyasu, K.; Mizuta, Y. P.; Matsuura, M.; Aoyama, K.; Kawamura, H. Observation of topological Z_2 vortex fluctuations in the frustrated Heisenberg magnet $NaCrO_2$. *Phys. Rev. B* **2022**, *106*, 054407.
[23] Rincón, C.; Torrres, T. E.; Sagredo, V.; Jiménez-Sandoval, S. J.; Mares-Jacinto, E. The fundamental absorption edge in $MnIn_2Se_4$ layer semi-magnetic semiconductor. *Phys. B: Condens. Matter* **2015**, *477*, 123–128.
[24] Rincón, C. G. Effect of the paramagnetic to spin-glass phase transition on the fundamental absorption edge of $MnIn_2Se_4$ magnetic semiconducting compound. *Rev. Mex. Fís.* **2019**, *65*, 14–19.
[25] Serra, M.; Antonatos, N.; Lajaunie, L.; Albero, J.; Garcia, H.; Weng, M. Y.; Bastonero, L.; Sarkar, K. J.; Gusmão, R.; Luxa, J. et al. A photodetector based on the non-centrosymmetric 2D pseudo-binary chalcogenide $MnIn_2Se_4$. *J. Mater. Chem. C* **2025**, *13*, 5356–5369.
[26] Tovar, R.; Quintero, M.; Quintero, E.; Bocaranda, P.; Ruiz, J.; More, A. E.; Höeger, L.; Briceño, J. M. Magnetic behaviour for the $MnIn_{2(1-z)}Ga_{2z}Se_4$ alloys. *Phys. Status Solidi B* **2000**, *220*, 435–439.
[27] Mantilla, J.; Ter Haar, E.; Coaquira, J. A. H.; Bindilatti, V. Experimental evidence of the spin-glass transition in the diluted magnetic semiconductor $Zn_{1-x}Mn_xIn_2Se_4$. *J. Phys.: Condens. Matter* **2008**, *20*, 455211.
[28] Mantilla Ochoa, J. C.; Bindilatti, V.; ter Haar, E.; Coaquira, J. A. H.; de Souza Brito, G. E.; Gratens, X.; Sagredo, V. Spin glass behavior in $MnIn_2Se_4$ and $Zn_{1-x}Mn_xIn_2Se_4$ magnetic semiconductors. *J. Magn. Magn. Mater.* **2004**, *272–276*, 1308–1309.
[29] Cui, J.; Boström, E. V.; Ozerov, M.; Wu, F. L.; Jiang, Q. N.; Chu, J. H.; Li, C. C.; Liu, F. C.; Xu, X. D.; Rubio, A. et al. Chirality selective magnon–phonon hybridization and magnon-induced chiral phonons in a layered zigzag antiferromagnet. *Nat. Commun.* **2023**, *14*, 3396.
[30] Inoue, K.; Okuno, M. Coherent anti-Stokes hyper-Raman spectroscopy. *Nat. Commun.* **2025**, *16*, 306.
[31] Yao, F. R.; Multian, V.; Wang, Z.; Ubrig, N.; Teyssier, J.; Wu, F.; Giannini, E.; Gibertini, M.; Gutiérrez-Lezama, I.; Morpurgo, A. F. Multiple antiferromagnetic phases and magnetic anisotropy in exfoliated $CrBr_3$ multilayers. *Nat. Commun.* **2023**, *14*, 4969.
[32] Song, Q.; Occhialini, C. A.; Ergeçen, E.; Ilyas, B.; Amoroso, D.; Barone, P.; Kapeghian, J.; Watanabe, K.; Taniguchi, T.; Botana, A. S. et al. Evidence for a single-layer van der Waals multiferroic. *Nature* **2022**, *602*, 601–605.
[33] Döll, G.; Anghel, A.; Baumann, J. R.; Bucher, E.; Ramirez, A. P.; Range, K. J. Structural and magnetic properties of the ternary manganese compound semiconductors $MnAl_2Te_4$, $MnIn_2Te_4$, and $MnIn_2Se_4$. *Phys. Status Solidi A* **1991**, *126*, 237–244.
[34] Tovar, R.; Quintero, M.; Quintero, E.; Bocaranda, P.; Ruiz, J.; Cadenas, R.; Mora, A. E.; Höeger, L.; Briceño, J. M.; Rakoto, H. et al. Crystallographic characterization and magnetic properties of the $MnIn_{2(1-z)}Ga_{2z}Se_4$ alloy system. *Mater. Res. Bull.* **2002**, *37*, 1011–1022.
[35] Zhai, Y. Q.; Deng, Y. F.; Fu, Z. D.; Feng, E. X.; Su, Y. X.; Shiga, T.; Oshio, H.; Zheng, Y. Z. Reentrant spin glass and large coercive field observed in a spin integer dimerized honeycomb lattice. *Adv. Funct. Mater.* **2021**, *31*, 2004744.
[36] Lemke, N.; Campbell, I. A. Two-dimensional Ising spin glasses with nonzero ordering temperatures. *Phys. Rev. Lett.* **1996**, *76*, 4616–4619.
[37] Jörg, T.; Katzgraber, H. G. Evidence for universal scaling in the spin-glass phase. *Phys. Rev. Lett.* **2008**, *101*, 197205.
[38] Sibille, R.; Gauthier, N.; Lhotel, E.; Porée, V.; Pomjakushin, V.; Ewings, R. A.; Perring, T. G.; Ollivier, J.; Wildes, A.; Ritter, C. et al. A quantum liquid of magnetic octupoles on the pyrochlore lattice. *Nat. Phys.* **2020**, *16*, 546–552.
[39] Wiebe, C. R.; Janik, J. A.; MacDougall, G. J.; Luke, G. M.; Garrett, J. D.; Zhou, H. D.; Jo, Y. J.; Balicas, L.; Qiu, Y.; Copley, J. R. D. et al. Gapped itinerant spin excitations account for missing entropy in the hidden-order state of URu_2Si_2. *Nat. Phys.* **2007**, *3*, 96–99.
[40] Kresse, G.; Furthmüller, J. Efficiency of *ab-initio* total energy calculations for metals and semiconductors using a plane-wave basis set. *Comput. Mater. Sci.* **1996**, *6*, 15–50.
[41] Blöchl, P. E. Projector augmented-wave method. *Phys. Rev. B* **1994**, *50*, 17953–17979.
[42] Kresse, J, G.; Furthmüller, J. Efficient iterative schemes for *ab initio* total-energy calculations using a plane-wave basis set. *Phys. Rev. B* **1996**, *54*, 11169–11186.
[43] Kim, K.; Lim, S. Y.; Lee, J. U.; Lee, S.; Kim, T. Y.; Park, K.; Jeon, G. S.; Park, C. H.; Park, J. G.; Cheong, H. Suppression of magnetic ordering in XXZ-type antiferromagnetic monolayer $NiPS_3$. *Nat. Commun.* **2019**, *10*, 345.
[44] Lyu, B.; Gao, Y. F.; Zhang, Y. J.; Wang, L.; Wu, X. H.; Chen, Y. N.; Zhang, J. S.; Li, G. M.; Huang, Q. L.; Zhang, N. P. et al. Probing the ferromagnetism and spin wave gap in VI_3 by helicity-resolved Raman spectroscopy. *Nano Lett.* **2020**, *20*, 6024–6031.
[45] Sheng, J. M.; Mei, J. W.; Wang, L.; Xu, X. Y.; Jiang, W. R.; Xu, L.; Ge, H.; Zhao, N.; Li, T. T.; Candini, A. et al. Bose–Einstein condensation of a two-magnon bound state in a spin-1 triangular lattice. *Nat. Mater.* **2025**, *24*, 544–551.
[46] Wulferding, D.; Choi, Y.; Do, S. H.; Lee, C. H.; Lemmens, P.; Faugeras, C.; Gallais, Y.; Choi, K. Y. Magnon bound states versus anyonic Majorana excitations in the Kitaev honeycomb magnet α-$RuCl_3$. *Nat. Commun.* **2020**, *11*, 1603.
[47] Li, G. M.; Chen, X. B.; Gan, Y.; Li, F. L.; Yan, M. Q.; Ye, F.; Pei, S. H.; Zhang, Y. J.; Wang, L.; Su, H. M. et al. Raman spectroscopy evidence for dimerization and Mott collapse in α-$RuCl_3$ under pressures. *Phys. Rev. Mater.* **2019**, *3*, 023601.
[48] Sandilands, L. J.; Tian, Y.; Plumb, K. W.; Kim, Y. J.; Burch, K. S. Scattering continuum and possible fractionalized excitations in α-$RuCl_3$. *Phys. Rev. Lett.* **2015**, *114*, 147201.
[49] Fano, U. Effects of configuration interaction on intensities and phase shifts. *Phys. Rev.* **1961**, *124*, 1866–1878.

This is an open access article under the terms of the Creative Commons Attribution 4.0 International License (CC BY 4.0, https://creativecommons.org/licenses/by/4.0/).

© The Author(s) 2026. Published by Tsinghua University Press.